

TiN 对激光焊接 TiAl 基合金相变组织及晶粒细化的影响

王梦飞^{1,2}, 刘捷^{1,2*}, 彭勇^{1,2}, 王克鸿^{1,2}¹南京理工大学受控电弧智能增材技术工信部重点实验室, 江苏 南京 210094;²南京理工大学材料科学与工程学院, 江苏 南京 210094

摘要 针对 TiAl 基合金激光焊接过程中出现的裂纹问题, 利用扫描电镜 (SEM) 及电子背散射衍射 (EBSD) 等方法研究了 TiN 相对接头焊缝相变组织及晶粒细化的影响。研究表明: 当焊缝中没有 TiN 相时, 焊接接头成形良好且没有缺陷, 焊缝组织主要为 Burgers α_2 相, 焊缝区域的完整凝固路径为 $L \rightarrow L + \beta \rightarrow \beta + \alpha \rightarrow \alpha + \gamma \rightarrow \alpha_2 + \gamma$; 当焊缝中存在 TiN 相时, 焊接接头产生了贯穿性裂纹缺陷, 主要原因是 TiN 是一种脆硬相, 在激光焊接过程中极易引发裂纹。焊缝组织主要由 TiN 枝晶相及 non-Burgers α_2 相组成, 同时 TiN 相和 α_2 相之间存在一定的取向关系即 $\{111\}_{\text{TiN}} // \{0001\}_{\alpha_2}$ 。TiN 相对焊缝组织有晶粒细化作用。焊缝区域的完整凝固路径为 $L \rightarrow \text{TiN} + L \rightarrow \text{TiN} + \beta \rightarrow \text{TiN} + \alpha + \gamma \rightarrow \text{TiN} + \alpha_2 + \gamma$ 。

关键词 激光技术; TiAl 合金; 激光焊接; 微观组织; 相变组织; 晶粒细化

中图分类号 TG442

文献标志码 A

DOI: 10.3788/CJL202249.1602015

1 引言

γ -TiAl 基合金具有低密度、抗氧化和高比强度等优点, 是航空航天领域中替代镍基高温合金的理想材料^[1-5]。然而, TiAl 合金的室温塑性和成形性较差, 焊接时极易产生裂纹, 其应用受到限制^[6-8]。目前, TiAl 合金的连接工艺主要包括氩弧焊^[9-10]、扩散焊^[11-12]、激光焊^[13-14]和电子束焊^[15-17]等。激光焊接方法因其高度的灵活性和适应性被广泛应用于各种材料的连接^[18-20], 但是 TiAl 基合金激光焊接时由于冷却速度快, 易产生大量的 α_2 脆硬相, 接头在焊接残余应力的作用下发生开裂。为了改善焊缝组织, 降低接头冷却速度, 国内外学者开展了大量的研究工作, 并取得了一定的进展。Chaturvedi 等^[17]通过改变焊前预热温度及焊接参数来控制焊缝的冷却速度, 系统研究了 TiAl 基合金电子束焊接时焊缝冷却速度对焊接裂纹的影响, 结果表明, 当焊接冷却速度低于 $250 \text{ }^\circ\text{C}/\text{s}$ 时, 焊缝中脆硬的 α_2 相转变为块状 γ 相和层片组织, 接头中无焊接裂纹出现, 但是焊前预热会导致元素偏析和晶粒粗大。Liu 等^[13]对焊前预热的 TiAl 激光焊接接头进行焊后原位热处理, 得到了无裂纹的接头; 同时发现, 在慢速冷却的条件下, 硼化物对晶粒细化起到了重要的作用。晶粒细化可以提高 TiAl 合金在室温和高温下的塑性, 在 TiAl 合金 $\beta \rightarrow \alpha$ 的相变过程中, 硼化物的形成对晶粒细化起着重要作用。目前, 国内外学者的

研究主要集中于硼化物对 TiAl 合金晶粒细化及相变组织的影响^[21-23], 关于 TiN 相在 TiAl 合金相变过程中的作用研究鲜有报道。

针对 TiAl 合金的连接问题, 本文通过扫描电镜 (SEM)、X 射线衍射 (XRD) 及电子背散射衍射 (EBSD) 等分析方法, 研究了焊接过程中 TiN 相的生成对 TiAl 合金激光焊接焊缝相变组织及晶粒细化的影响。

2 试验方法

试验材料采用化学成分 (原子数分数) 为 Ti (53.3%) + Al (42%) + Cr (2.5%) + Nb (1%) + Si (0.7%) + B (0.5%) 的 γ -TiAl 合金。通过电火花加工 (EDM) 将 TiAl 铸锭切割成尺寸为 $20 \text{ mm} \times 20 \text{ mm} \times 2.5 \text{ mm}$ 的板材。本试验采用的激光器为 IPG 公司生产的 IPG-10000W 光纤激光器, 输出波长为 $(1070 \pm 10) \text{ nm}$, 激光束通过光纤传导至激光焊接头中。激光焊接头被连接在德国 KUKA 焊接机器人上, 重复定位精确度达到 $\pm 0.1 \text{ mm}$ 。激光焊接设备及焊接过程示意图如图 1 所示。焊接过程中采用的激光功率为 5 kW , 焊接速度为 $6 \text{ m}/\text{min}$ 。

在焊接试验前, 用 800 # SiC 砂纸打磨去除 TiAl 合金板材表面的氧化物和加工残留物, 然后用丙酮和乙醇清洗晾干。焊接时为了防止氧化, 分别使用氮气和氩气作为保护气。焊接结束后, 沿垂直于焊缝方向

收稿日期: 2021-11-22; 修回日期: 2021-12-13; 录用日期: 2021-12-31

基金项目: 江苏省自然科学基金 (BK20200502)

通信作者: *j.liu@njjust.edu.cn

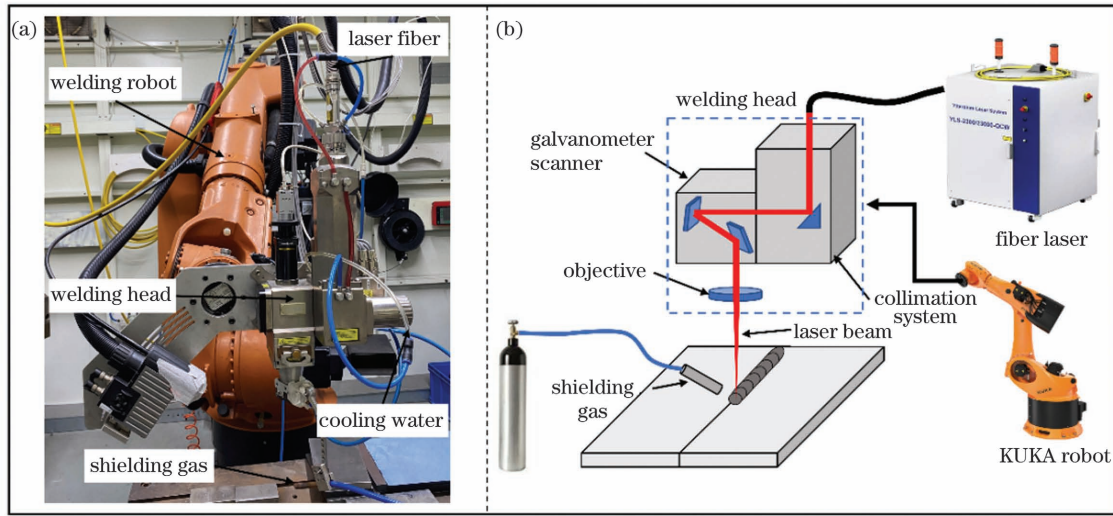


图 1 试验设备及焊接过程示意图

Fig. 1 Experimental equipment and schematic of welding process

切取金相样,经研磨和抛光处理后进行微观组织分析。采用 FEI Quanta-200 场发射扫描电子显微镜在背散射(BSE)模式下观察焊接接头的微观组织,采用电子背散射衍射对其微观组织取向关系进行分析。

3 试验结果与分析

3.1 显微组织与相确定

图 2 所示为分别使用氮气与氩气作为保护气时激

光焊接得到的接头横截面形貌。图 2(a)所示为使用氮气作为保护气时焊接得到的接头,接头内部产生了明显的贯穿性裂纹,焊缝表面成形较差,有裂纹缺陷。而使用氩气作为保护气时得到了无裂纹的焊接接头[图 2(b)],且焊缝表面成形良好,焊缝整体呈“X”形,焊接接头完全熔透。由于焊接过程中使用的焊接参数完全相同,因此推测是保护气对焊缝的组织 and 性能产生了影响。

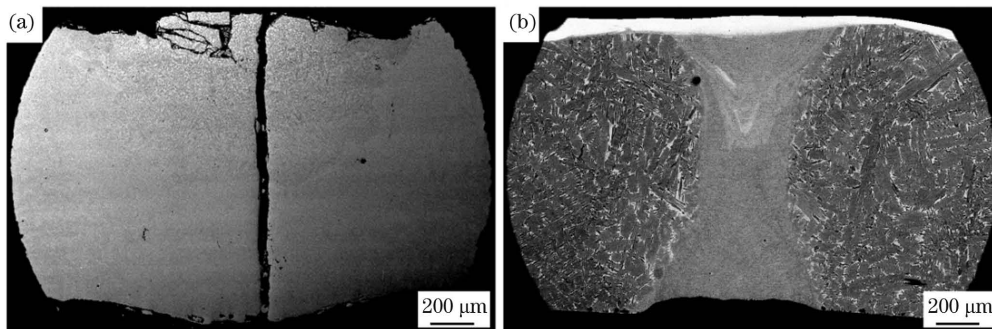


图 2 不同保护气下得到的焊缝接头横截面形貌。(a)氮气;(b)氩气

Fig. 2 Cross-sectional morphologies of joints welded under different shielding gases. (a) Nitrogen; (b) argon

根据 Ti-Al 二元相图(图 3)可知,焊接过程中发生的凝固路径为 $L \rightarrow L + \beta \rightarrow \beta + \alpha \rightarrow \alpha + \gamma \rightarrow \alpha_2 + \gamma$ 。图 4 为分别使用氮气和氩气作为保护气时得到的接头焊缝的微观组织高倍数 SEM 图(背散射模式)。氮气作为保护气时,焊接接头的焊缝上部与下部呈现出不同的组织特征,上部与下部区域的典型微观组织如图 4(a)、(b)所示。可以看出,接头上部区域的组织为枝晶组织,而接头下部由大量板条状组织组成,不存在枝晶形貌组织。图 4(c)、(d)为氩气作为保护气时焊接得到的接头焊缝组织,接头上下部的组织形貌一致,都为板条状组织,黑灰色的板条组织被亮白色隔开。

图4(b)~(d)呈现为明显的板条状组织特征,这

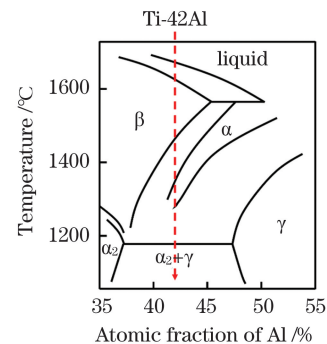


图 3 Ti-Al 二元相图

Fig. 3 Ti-Al binary phase diagram

样的组织形貌与其他学者进行 TiAl 合金激光焊接时得到的焊缝组织形貌一致^[13-14],焊缝组织由取向不同

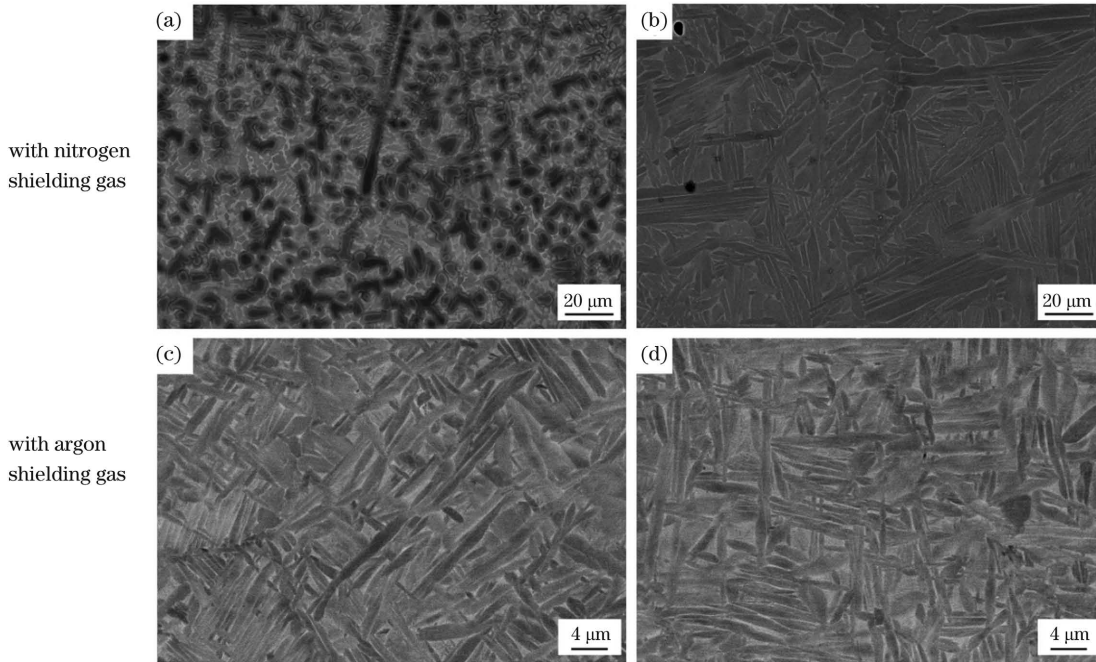


图 4 不同保护气下得到的焊缝接头的微观组织。(a)(c)上部;(b)(d)下部

Fig. 4 Microstructures of joints welded under different shielding gases. (a) (c)Top area; (b) (d)bottom area

的板条状 α_2 相和 γ 相组成。通过能谱仪(EDS)检测发现,在 $\beta \rightarrow \alpha$ 的转变过程中,Cr、Nb 等元素被排出到板条状 α_2 相的边界处,因此在板条状 α_2 相之间呈亮白色。

为了进一步确定相的组成,分别对两种保护气下得到的接头上下部区域进行微区 XRD 试验,结果如图 5 所示。可以看出,当氮气作为保护气时,焊缝上部区域存在 TiN 相,而焊缝下部区域以及氩气作为保护气时的焊缝的相组成都为 α_2 -Ti₃Al 相和 γ -TiAl 相。对焊缝上部区域的枝晶进行 EDS 线扫描分析(图 6),发现 N 元素在枝晶内部富集,同时枝晶内部贫 Al。因此结合 XRD 结果分析可知,焊缝上部区域的枝晶相为 TiN。通过查阅文献发现,在氮气保护下得到的接头的上部区域组织形貌与激光气体渗氮工艺得到的组织形貌类似^[24-27]。由于 Ti 是强烈的固氮元素,在焊接过程中,氮气流覆盖在熔池表面上,高温金属熔液表面

吸附氮元素,氮气的溶解使得熔池的上部产生贫铝层。当氮气进入高温合金液中时,氮元素与熔池中的钛元素发生剧烈的冶金反应生成氮化钛。由此可以确定,焊缝中的枝晶组织为 TiN 相,枝晶间为 Ti₃Al 相,晶界由于富集 Cr、Nb 等元素而呈现为亮白色。

3.2 EBSD 分析

图 7(a)、(b)所示为氮气接头下部区域 α_2 晶粒的反极图(IPF)和(0001)方向极图,其中 TD 表示横向, RD 表示轧向。焊缝下部区域由细小的针状 α_2 板条组成, α_2 相的体积分数为 88.13%。在 $\beta \rightarrow \alpha$ 的转变过程中,低温密排六方(hcp)结构的 α 相与高温体心立方(bcc)结构的 β 相之间将保持特定的晶体学位向关系,这种特殊的位向关系被称为柏格斯关系(Burgers relationship)^[28-29],即 $\{0001\}_\alpha // \{110\}_\beta$, $\langle 11\bar{2}0 \rangle_\alpha // \langle 111 \rangle_\beta$ 。正是由于这种特定位向关系的存在,同时考虑到晶体的对称性,次生的 α 相共有 12 种变体,而且

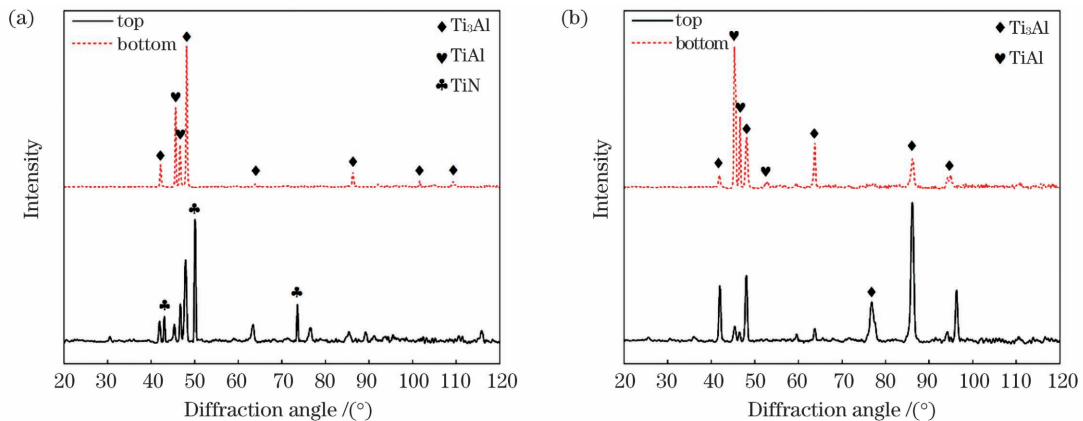


图 5 不同保护气下得到的焊缝接头的 XRD 图谱。(a)氮气;(b)氩气

Fig. 5 XRD patterns of joints welded under different shielding gases. (a) Nitrogen; (b) argon

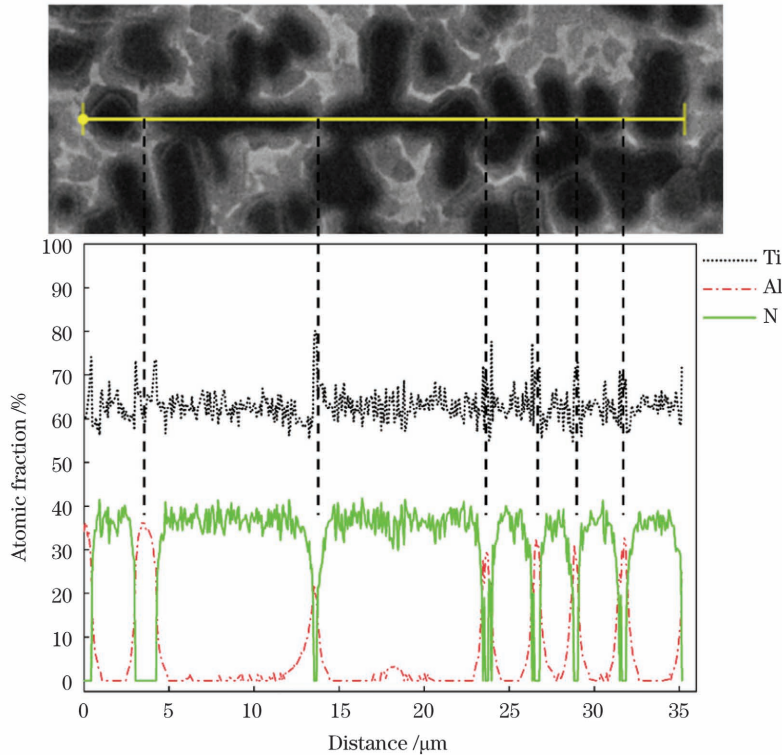


图 6 枝晶中的元素分布

Fig. 6 Elemental distribution in dendrites

根据 Gey 等^[30]的研究可知,来自同一个初生 β 晶粒的 12 种变体之间的取向差只能是 10.5° , 60° , 60.8° 和 90° 。因此根据 α_2 晶粒(0001)取向之间的取向差,图 7(a)中的 α_2 晶粒可以分为四组,如图 7(c)~(j)所示。各组 α_2 晶粒的体积分数分别为 29.4%、21%、9.2% 和 8.6%。同一组中的 α_2 晶粒{0001}晶面间的取向差均满足 $(10 \pm 2)^\circ$ 、 $(60 \pm 2)^\circ$ 和 $(90 \pm 2)^\circ$,因此这些 α_2 晶粒与初生 β 晶粒之间存在 Burgers 取向关系,它们均来自同一个初生 β 晶粒。这说明在 $\beta \rightarrow \alpha$ 的固态相变过程中, α 相的取向继承自初生 β 相,即 α 相以 β 相为核心形核生长,整个相变过程的凝固路径为 $L \rightarrow L + \beta \rightarrow \beta + \alpha \rightarrow \alpha + \gamma \rightarrow \alpha_2 + \gamma$ 。由于每组 α_2 晶粒存在上述关系,一组 α_2 晶粒形成一个束集,因此焊缝区域晶粒的大小不能简单地由 α_2 晶粒的尺寸来确定,而是依赖于每组束集的尺寸大小,粗化的束集组织抑制了针状 α_2 相的晶粒细化作用。

图 8(a)、(b)为氩气接头中 α_2 晶粒的 IPF 和 (0001)方向极图。同上文所述,根据 α_2 晶粒(0001)取向之间的取向差,氩气接头[图 8(a)]中的 α_2 晶粒也可以分为四组,如图 8(c)~(j)所示。每一组 α_2 晶粒之间都存在 $(10 \pm 2)^\circ$ 、 $(60 \pm 2)^\circ$ 和 $(90 \pm 2)^\circ$ 的取向关系,这说明 α_2 晶粒与初生 β 晶粒之间存在 Burgers 取向关系。因此证明当使用氩气作为保护气时,焊缝组织的凝固行为与氮气接头上部区域是一致的。

图 9 所示为氮气接头上部区域 α_2 晶粒的 IPF 和 (0001)方向极图, α_2 晶粒的取向十分分散,经过取向分析可知, α_2 晶粒之间不存在 10.5° 、 60° 、 60.8° 和

90° 的取向关系,这说明在氮气接头上部区域,发生 $\beta \rightarrow \alpha$ 转变时 β 相与 α 相之间没有保持 Burgers 取向关系。从图 9 中可以看出, α_2 晶粒在 TiN 枝晶间生成,这是由于 TiN 的熔点较高(2930°C ^[31]),在冷却过程中焊缝上部区域先析出 TiN 枝晶,在 TiN 凝固的后期,形成发达的 TiN 枝晶,Al、Nb、Cr 等元素被排出到枝晶间区域,随后枝晶间残余液相转变为初生 β 相。在随后的冷却过程中,发生 $\beta \rightarrow \alpha \rightarrow \alpha_2$ 转变。从图 9 中还可以看出, α_2 晶粒的尺寸非常细小,没有形成前文所述的束集组织,通过 iMage Pro 软件对图 8 中的束集组织进行测量,可得束集组织的平均大小为 $1451.38 \mu\text{m}^2$,而通过 EBSD 数据,提取的图 9 中的 α_2 晶粒大小约为 $47.48 \mu\text{m}^2$ 。因此对比得出, TiN 的生成对焊缝组织具有晶粒细化作用。

从 EBSD 数据中提取了一个完整 TiN 枝晶与其周围 α_2 晶粒的 TiN(111)和 α_2 (0001)取向,结果如图 10 所示,枝晶周围的 α_2 晶粒与 TiN 枝晶有一定的取向关系。图 10(b)、(c)分别为 TiN 相和 α_2 相的极图,可以看出, TiN 枝晶的(111)方向平行于 α_2 晶粒的(0001)方向,即 $\{111\}_{\text{TiN}} // \{0001\}_{\alpha_2}$ 。由此判断, α_2 相以 TiN 枝晶为形核核心,按照 $\{111\}_{\text{TiN}} // \{0001\}_{\alpha_2}$ 取向关系进行生长,打破了传统 $\beta \rightarrow \alpha$ 转变过程中的 Burgers 取向关系。因此,焊缝上部区域在焊接过程中的完整相变过程为首先析出 TiN 枝晶,之后以 TiN 枝晶为核心发生凝固路径为 $L \rightarrow \text{TiN} + L \rightarrow \text{TiN} + \beta \rightarrow \text{TiN} + \alpha + \gamma \rightarrow \text{TiN} + \alpha_2 + \gamma$ 的相变。

在 $\beta \rightarrow \alpha$ 的转变过程中, α 相可以通过 Burgers 关

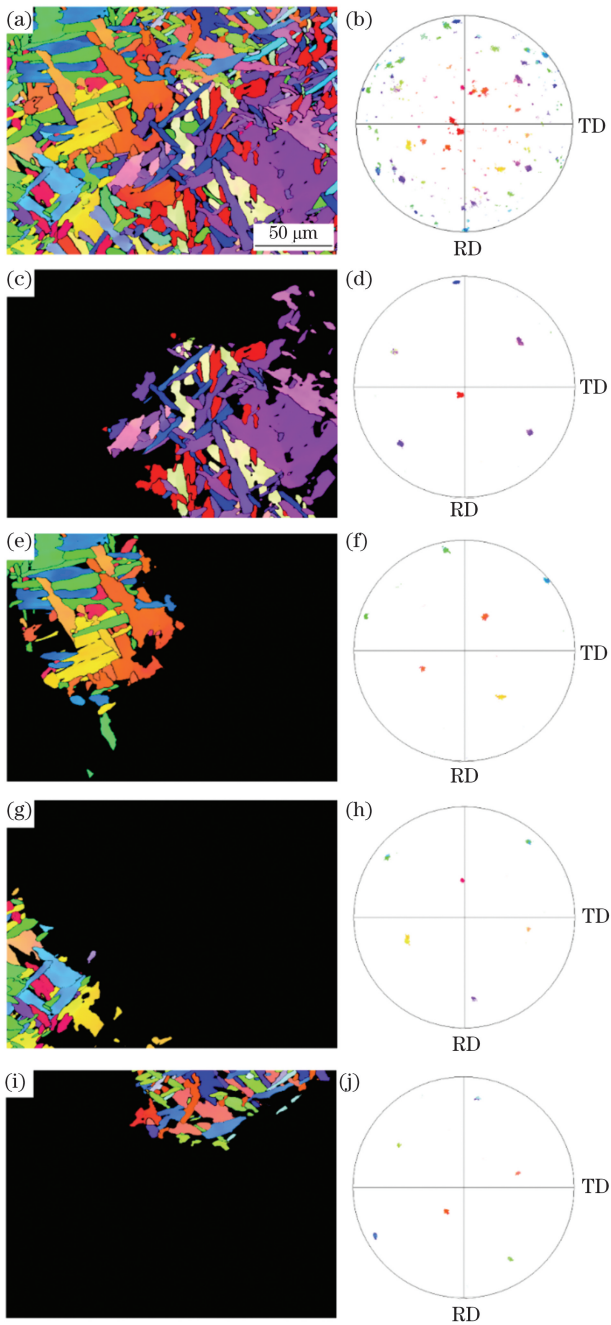


图 7 氮气下得到的焊缝接头下部区域 α_2 晶粒的 EBSD IPFs (左) 和 (0001) 方向极图 (右)。(a)(b) 所有 α_2 晶粒; (c)(d) 第一组 α_2 晶粒; (e)(f) 第二组 α_2 晶粒; (g)(h) 第三组 α_2 晶粒; (i)(j) 第四组 α_2 晶粒

Fig. 7 EBSD IPFs (left) and (0001) pole figures (right) of α_2 grains in bottom area of joint welded under nitrogen gas. (a)(b) Total α_2 grains; α_2 grains: (c)(d) group 1, (e)(f) group 2, (g)(h) group 3, (i)(j) group 4

系继承母相 β 相的取向, 或者前面提到的继承 TiN 相的取向。因此, 这两个取向关系存在竞争。在 α 相形核过程中, 如果选择 Burgers 取向关系, 那么由于 α 相

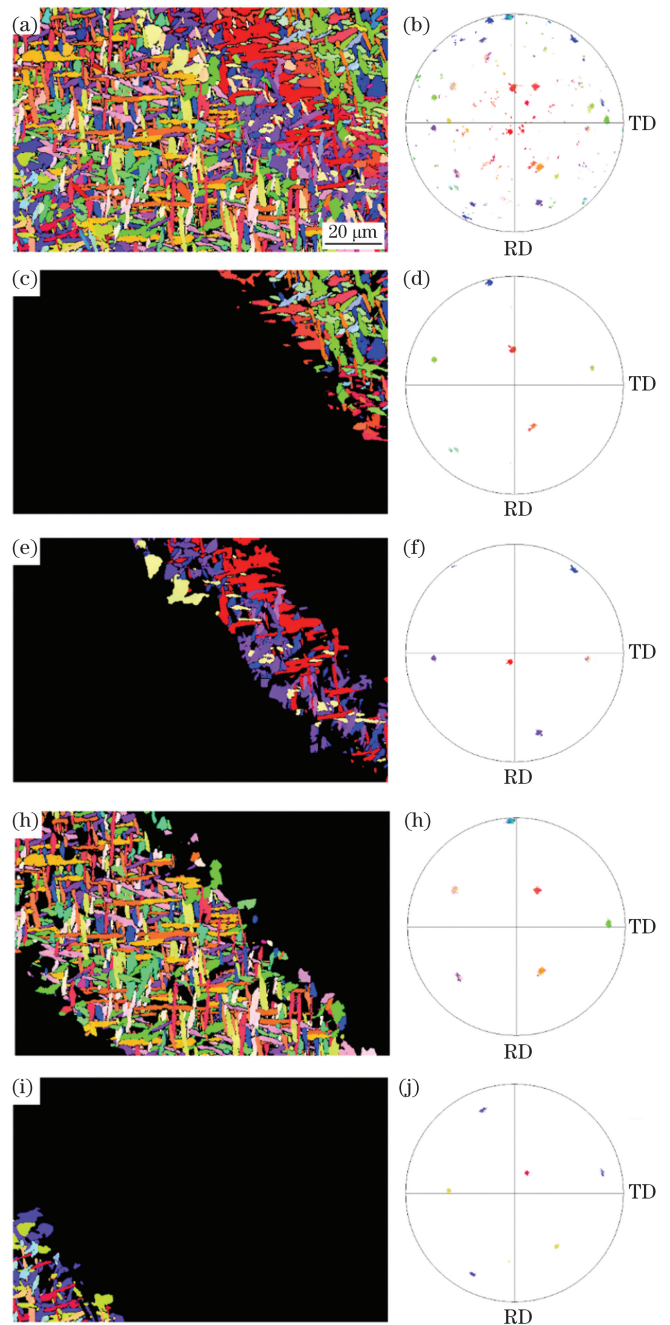


图 8 氩气下得到的焊缝接头 α_2 晶粒的 EBSD IPFs (左) 和 (0001) 方向极图 (右)。(a)(b) 所有 α_2 晶粒; (c)(d) 第一组 α_2 晶粒; (e)(f) 第二组 α_2 晶粒; (g)(h) 第三组 α_2 晶粒; (i)(j) 第四组 α_2 晶粒

Fig. 8 EBSD IPFs (left) and (0001) pole figures (right) of α_2 grains in joint welded under argon gas. (a)(b) Total α_2 grains; α_2 grains: (c)(d) group 1, (e)(f) group 2, (g)(h) group 3, (i)(j) group 4

和 β 相之间有比较高的错配度, 形核将比较困难。而 TiN 枝晶相当于一种孕育剂, 以 TiN 枝晶作为形核核心可以降低高的形核能。

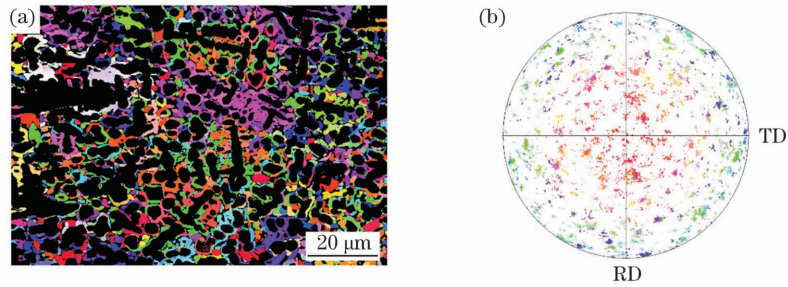


图 9 氮气接头上部区域 α_2 晶粒的 EBSD 分析结果。(a)IPF;(b)(0001)方向极图

Fig. 9 EBSD analysis results of α_2 grains in top area of joint welded under nitrogen gas. (a) IPF; (b) (0001) pole figure

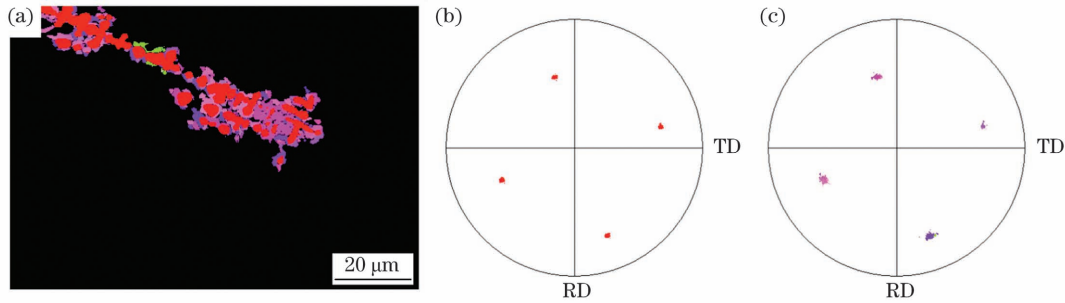


图 10 TiN 枝晶和 α_2 晶粒的 EBSD 分析结果。(a)TiN 枝晶和 α_2 晶粒的 IPF;(b)TiN 枝晶的(111)方向极图;(c) α_2 晶粒的(0001)方向极图

Fig. 10 EBSD analysis results of TiN dendrite and α_2 grains. (a) IPF of TiN dendrite and α_2 grains; (b) (111) pole figure of TiN dendrite; (c) (0001) pole figure of α_2 grains

建立了 α 相以 TiN 枝晶为形核核心的生长模型, 如图 11(b)所示。当 TiAl 基合金相变过程中不存在 TiN 相时,如图 11(a)所示, $\beta \rightarrow \alpha$ 的相变过程为针状 α 晶粒在 β 晶界处形核并向 β 晶内长大,因此 α 相与母相 β 相存在 Burgers 取向关系(OR)^[28-29],并且存在 12 种变体。当相变过程中存在 TiN 相时,如图 11(b)所示, α 相以 TiN 枝晶为形核核心生长, α 相与 TiN 枝晶之间保持一种固定的取向关系,即 $\{111\}_{TiN} // \{0001\}_{\alpha_2}$ 。

本次试验证明了 TiN 相作为孕育剂起到细化晶粒的作用,这有助于提高 TiAl 合金在室温和高温下的塑性,为推进 TiAl 基合金在工业中的实际应用提供了理论支持及技术参考。此外,TiN 相的存在将 $\beta \rightarrow \alpha$ 转变过程中具有 12 种变体的 Burgers 取向关系转变为一种确定的 $\{111\}_{TiN} // \{0001\}_{\alpha_2}$ 取向关系,实现了 $\beta \rightarrow \alpha$ 的定向固态相变,因此有望以 TiN 为籽晶进行 TiAl 单晶的定向凝固制造。

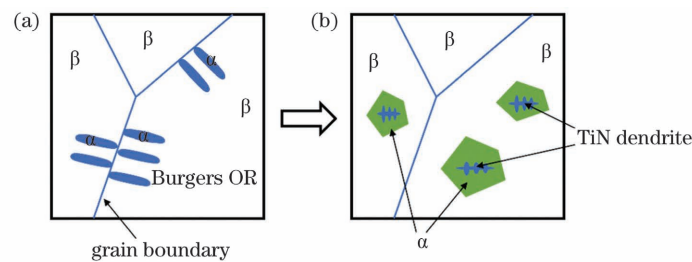


图 11 α 相的生长机制示意图。(a)在 β 晶界上形核的针状 α 晶粒;(b)以 TiN 枝晶为形核核心生长的等轴 α 晶粒

Fig. 11 Schematics of growth mechanism of α phase. (a) Acicular α grains nucleated on β grain boundary; (b) equiaxed α grains grown with TiN dendrites as nucleation cores

4 结 论

以 Ti-42Al-2.5Cr-1Nb-0.7Si-0.5B 合金作为研究对象,开展了不同保护气下激光焊接的研究。对合金进行了激光焊接试验,分析研究了 TiN 相对激光焊接接头微观组织及晶粒细化的影响,得出如下结论。

1)在激光焊接 TiAl 基合金时,使用氮气和氩气作为保护气会对焊缝组织与性能产生很大影响。使用氩

气焊接 TiAl 基合金时,焊接过程稳定,可以获得成形良好且无裂纹的焊接接头;使用氮气焊接 TiAl 基合金时,会发生渗氮现象,氮元素进入熔池形成 TiN 枝晶,由于 TiN 是脆硬的陶瓷相,接头容易产生贯穿性裂纹。

2)氮气作为保护气时,会改变熔池液态金属传统的凝固路径。在焊接过程中,氮元素进入熔池,首先生成 TiN 枝晶,在随后的冷却过程中, $\beta \rightarrow \alpha$ 的转变以

TiN 枝晶为核心,从而打破了传统的 Burgers 取向关系,形成 $\{111\}_{\text{TiN}} // \{0001\}_{\alpha_2}$ 的取向关系。同时, TiN 的生成对焊缝组织起到晶粒细化的作用。焊接过程中液态金属冷却的完整凝固路径为 $L \rightarrow \text{TiN} + L \rightarrow \text{TiN} + \beta \rightarrow \text{TiN} + \alpha + \gamma \rightarrow \text{TiN} + \alpha_2 + \gamma$ 。

参 考 文 献

- [1] Kim Y W. Ordered intermetallic alloys, part III: gamma titanium aluminides[J]. JOM, 1994, 46(7): 30-39.
- [2] Clemens H, Kestler H. Processing and applications of intermetallic γ -TiAl-based alloys [J]. Advanced Engineering Materials, 2000, 2(9): 551-570.
- [3] Clemens H, Mayer S. Design, processing, microstructure, properties, and applications of advanced intermetallic TiAl alloys [J]. Advanced Engineering Materials, 2013, 15(4): 191-215.
- [4] Cheng J, Li F, Zhu S Y, et al. Electrochemical corrosion and tribological evaluation of TiAl alloy for marine application[J]. Tribology International, 2017, 115: 483-492.
- [5] Gussone J, Garces G, Haubrich J, et al. Microstructure stability of γ -TiAl produced by selective laser melting [J]. Scripta Materialia, 2017, 130: 110-113.
- [6] Nishikiori S, Matsuda K, Nakagawa Y G. Microstructural effects on tensile properties of cast TiAl-Fe-V-B alloy [J]. Materials Science and Engineering: A, 1997, 239/240: 592-599.
- [7] Fergus J W. Review of the effect of alloy composition on the growth rates of scales formed during oxidation of gamma titanium aluminide alloys [J]. Materials Science and Engineering: A, 2002, 338(1/2): 108-125.
- [8] Naveed M, Renteria A F, Weiß S. Role of alloying elements during thermocyclic oxidation of β/γ -TiAl alloys at high temperatures[J]. Journal of Alloys and Compounds, 2017, 691: 489-497.
- [9] Bharani D J, Acoff V L. Autogenous gas tungsten arc weldability of cast alloy Ti-48Al-2Cr-2Nb (atomic percent) versus extruded alloy Ti-46Al-2Cr-2Nb-0.9Mo (atomic percent) [J]. Metallurgical and Materials Transactions A, 1998, 29(3): 927-935.
- [10] Arenas M F, Acoff V L. Analysis of gamma titanium aluminide welds produced by gas tungsten arc welding [J]. Welding Journal, 2003, 82(5): 110S.
- [11] Duarte L I, Viana F, Ramos A S, et al. Diffusion bonding of gamma-TiAl using modified Ti/Al nanolayers [J]. Journal of Alloys and Compounds, 2012, 536: S424-S427.
- [12] Du Z H, Zhang K F, Lu Z, et al. Microstructure and mechanical properties of vacuum diffusion bonding joints for γ -TiAl based alloy[J]. Vacuum, 2018, 150: 96-104.
- [13] Liu J, Dahmen M, Ventske V, et al. The effect of heat treatment on crack control and grain refinement in laser beam welded β -solidifying TiAl-based alloy[J]. Intermetallics, 2013, 40: 65-70.
- [14] Liu J, Staron P, Riekehr S, et al. In situ study of phase transformations during laser-beam welding of a TiAl alloy for grain refinement and mechanical property optimization [J]. Intermetallics, 2015, 62: 27-35.
- [15] Chaturvedi M C, Xu Q, Richards N L. Development of crack-free welds in a TiAl-based alloy [J]. Journal of Materials Processing Technology, 2001, 118(1/2/3): 74-78.
- [16] Chen G Q, Zhang B G, Liu W, et al. Crack formation and control upon the electron beam welding of TiAl-based alloys[J]. Intermetallics, 2011, 19(12): 1857-1863.
- [17] Chaturvedi M C, Richards N L, Xu Q. Electron beam welding of a Ti-45Al-2Nb-2Mn+0.8 vol. % TiB₂ XD alloy[J]. Materials Science and Engineering: A, 1997, 239/240: 605-612.
- [18] 翟战江, 赵琳, 彭云, 等. DP980 钢激光焊接接头的低周疲劳性能[J]. 中国激光, 2021, 48(18): 1802003.
Zhai Z J, Zhao L, Peng Y, et al. Low cycle fatigue behavior of laser welded DP980 steel joints[J]. Chinese Journal of Lasers, 2021, 48(18): 1802003.
- [19] 陈根余, 钟沛新, 程少祥. 玻璃激光焊接过程中玻璃料与基板的耦合行为[J]. 中国激光, 2021, 48(18): 1802005.
Chen G Y, Zhong P X, Cheng S X. Coupling behavior between glass frit and plate during laser-assisted glass frit bonding[J]. Chinese Journal of Lasers, 2021, 48(18): 1802005.
- [20] 张迪, 赵琳, 刘奥博, 等. 激光能量对激光焊接接头熔化形状、气孔和微观组织的影响及其调控方法[J]. 中国激光, 2021, 48(15): 1502005.
Zhang D, Zhao L, Liu A B, et al. Understanding and controlling the influence of laser energy on penetration, porosity, and microstructure during laser welding[J]. Chinese Journal of Lasers, 2021, 48(15): 1502005.
- [21] Yang C, Jiang H, Hu D, et al. Effect of boron concentration on phase transformation texture in as-solidified Ti₄₄Al₈Nb₂B[J]. Scripta Materialia, 2012, 67(1): 85-88.
- [22] Liu J, Wu T L, Wang M F, et al. In situ observation of competitive growth of α grains during $\beta \rightarrow \alpha$ transformation in laser beam manufactured TiAl alloys [J]. Materials Characterization, 2021, 179: 111371.
- [23] Hu D W. Role of boron in TiAl alloy development: a review[J]. Rare Metals, 2016, 35(1): 1-14.
- [24] Nwobu A I P, Rawlings R D, West D R F. Nitride formation in titanium based substrates during laser surface melting in nitrogen-argon atmospheres[J]. Acta Materialia, 1999, 47(2): 631-643.
- [25] 刘常升, 陈岁元, 尚丽娟, 等. 铸态 γ -TiAl 合金的激光气相渗氮组织[J]. 金属热处理, 2001, 26(4): 1-4.
Liu C S, Chen S Y, Shang L J, et al. Microstructure of laser gas nitriding layer on γ -TiAl casting alloy[J]. Heat Treatment of Metals, 2001, 26(4): 1-4.
- [26] Fu Y, Zhang X C, Sui J F, et al. Microstructure and wear resistance of one-step *in situ* synthesized TiN/Al composite coatings on Ti₆Al₄V alloy by a laser nitriding process[J]. Optics & Laser Technology, 2015, 67: 78-85.
- [27] 顾玉芬, 耿培彪, 石玟, 等. 光纤激光氮化处理对 TC4 合金组织和性能的影响[J]. 兰州理工大学学报, 2020, 46(4): 10-14.
Gu Y F, Geng P B, Shi Y, et al. Effect of laser power on microstructure and properties of laser nitriding layer of TC4 alloy[J]. Journal of Lanzhou University of Technology, 2020, 46(4): 10-14.
- [28] Burgers W G. On the process of transition of the cubic-body-centered modification into the hexagonal-close-packed modification of zirconium [J]. Physica, 1934, 1(7/8/9/10/11/12): 561-586.
- [29] Furuhashi T, Takagi S, Watanabe H, et al. Crystallography of grain boundary α precipitates in a β titanium alloy [J]. Metallurgical and Materials Transactions A, 1996, 27(6): 1635-1646.
- [30] Gey N, Humbert M. Characterization of the variant selection occurring during the $\alpha \rightarrow \beta \rightarrow \alpha$ phase transformations of a cold rolled titanium sheet [J]. Acta Materialia, 2002, 50(2): 277-287.
- [31] Li W, Guler U, Kinsey N, et al. Refractory plasmonics with titanium nitride: broadband metamaterial absorber [J]. Advanced Materials, 2014, 26(47): 7959-7965.

Effect of TiN on Phase Transformation, Texture and Grain Refinement in Laser Beam Welded TiAl-Based Alloy

Wang Mengfei^{1,2}, Liu Jie^{1,2*}, Peng Yong^{1,2}, Wang Kehong^{1,2}

¹Key Laboratory of Controlled Arc Intelligent Additive Manufacturing Technology, Ministry of Industry and Information Technology, Nanjing University of Science and Technology, Nanjing 210094, Jiangsu, China;

²School of Materials Science and Engineering, Nanjing University of Science and Technology, Nanjing 210094, Jiangsu, China

Abstract

Objective The intermetallic γ -TiAl-based alloy, as a new type of lightweight high-temperature structural material, has the advantages of low density (3.9–4.2 g/cm³), high melting point, high strength, good oxidation resistance, and excellent creep at elevated temperature, and has gained wide attention in the application of high-temperature structural parts for aerospace vehicles and automobile engines. Since in practical applications, such as turbine blades, automotive turbochargers, and exhaust valves, the TiAl-based alloy needs to be connected to its own components or dissimilar metals and the research and development of the connection technology have become the key to the promotion and application of TiAl-based alloy. Diffusion bonding, argon-arc welding, infrared brazing, friction welding, laser beam welding and electron beam welding have been investigated with the aim of producing sound TiAl joints. However, the intrinsic brittleness of TiAl-based alloy often results in cracks, high residual stress, and poor mechanical properties of welds, limiting its more widespread applications in industry and commerce. Considering the poor plasticity of TiAl alloy, the control of welding cracks of TiAl-based alloy has become the keystone of the corresponding research.

Methods The γ -TiAl based alloy with a chemical composition of Ti-42Al-2.5Cr-1Nb-0.7Si-0.5B is investigated here. The Ti42 is prepared using plasma arc melting in the form of button ingot. The button ingot has been melted for 4 times to improve its homogeneity. The 20 mm × 20 mm × 2.5 mm plates are taken from the ingot by electro-discharge machining (EDM) and subsequently cleaned and ground with the 800 # SiC paper to remove oxides and machining remnants. The welding process is carried out with an IPG Ytterbium fiber laser, and a KUKA robot is used to control the laser beam movement in the x - y - z coordinate system. All plates have gone through three processes: pre-heating, welding, and post-weld heat treatment. The laser welding equipment and the welding process are shown in Fig. 1. The laser power used in the welding process is 5 kW, and the welding speed is 6 m/min. In order to prevent oxidation during welding, nitrogen and argon gases are used as shielding gases, and the effect of shielding gas on welding is investigated. The welds are visually inspected and investigated by X-ray radiographic inspection to detect cracks and porosity. The as-welded specimens are first sectioned, ground, and polished, and then mechanically polished with a vibrating polisher. The microstructure of the welded joint is observed using the FEI Quanta-200 field emission scanning electron microscope in the backscattering (BSE) mode, and the orientation relationship of its microstructure is analyzed using electron backscatter diffraction (EBSD).

Results and Discussions The joints welded under nitrogen shielding gas have obvious penetrating cracks inside the joints and the weld surface is poorly formed [Fig. 2(a)]. The use of argon gas as the shielding gas makes a crack-free welded joint realized. The weld surface is well formed, and the weld is in an “X” shape as a whole [Fig. 2(b)]. When nitrogen gas is used as the shielding gas, the TiN phase exists in the top area of the weld. The phase compositions in the bottom area of the weld are α_2 -Ti₃Al phase and γ -TiAl phase when argon gas is used as the shielding gas (Figs. 5 and 6). According to the Ti-Al binary phase diagram, there exists a transformation, $\beta \rightarrow \alpha$, in the alloy with Al concentration (atomic fraction) of 42% (Fig. 3). During the transformation from β to α , the α phase (hexagonal close-packed) and the β phase (body-centred cubic) maintain a specific crystal orientation relationship. This special orientation relationship is called the Burgers relationship, $\{0001\}_\alpha // \{110\}_\beta$ and $\langle 11\bar{2}0 \rangle_\alpha // \langle 111 \rangle_\beta$ (Figs. 7 and 8). The results indicate that when there is no TiN phase in the weld zone, the welded joint is formed well without defects, and the weld zone is composed of Burgers α_2 phase. The complete solidification path of the weld zone is $L \rightarrow L + \beta \rightarrow \beta + \alpha \rightarrow \alpha + \gamma \rightarrow \alpha_2 + \gamma$. When there is TiN phase in the weld zone, the welded joint produces penetrating crack defects. The main reason is that TiN is a brittle intermetallic compound, which can easily cause cracks during laser welding. The weld zone is mainly composed of TiN dendritic phase and non-Burgers α_2 phase. Moreover, there exists a certain orientation relationship between TiN phase and α_2 phase: $\{111\}_{\text{TiN}} // \{0001\}_{\alpha_2}$ (Fig. 10). The formation of TiN phase has a grain refinement effect on the weld structure. The complete solidification path of the weld zone is $L \rightarrow \text{TiN} + L \rightarrow \text{TiN} + \beta \rightarrow \text{TiN} + \alpha + \gamma \rightarrow \text{TiN} + \alpha_2 + \gamma$.

Conclusions A study on laser welding under different shielding gases is carried out with the Ti-42Al-2.5Cr-1Nb-0.7Si-0.5B alloy as the research object. A laser welding experiment is carried out with this alloy, and the effect of TiN on the phase transformation, texture, and grain refinement of laser welded joints is analyzed and studied. During laser welding of the TiAl-based alloy, the use of nitrogen and argon gases as shielding gases can have a great impact on the microstructure and properties. When using the argon gas, the welding process is stable, and a well-formed and crack-free welded joint is obtained. In contrast, when the nitrogen gas is used, nitrogen enters the melt pool to form the TiN dendrites, and penetration cracks can be easily produced in the joint because TiN is a brittle ceramic phase. The use of nitrogen gas as the shielding gas changes the traditional solidification path of the molten pool liquid metal. During the welding process, nitrogen enters the molten pool and the TiN dendrites are generated. In the subsequent cooling process, the $\beta \rightarrow \alpha$ transformation is centered on the TiN dendrites, thus breaking the traditional Burgers orientation relationship and forming the orientation relationship of $\{111\}_{\text{TiN}} // \{0001\}_{\alpha_2}$. At the same time, the generation of TiN has a grain refining effect on the weld organization. The complete solidification path of liquid metal cooling during the welding process is $L \rightarrow \text{TiN} + L \rightarrow \text{TiN} + \beta \rightarrow \text{TiN} + \alpha + \gamma \rightarrow \text{TiN} + \alpha_2 + \gamma$.

Key words laser technique; TiAl alloy; laser welding; microstructure; phase transformation texture; grain refinement